Li et al. *NPG Asia Materials* (2023) 15:3
https://doi.org/10.1038/s41427-022-00456-7

NPG Asia Materials

ARTICLE Open Access

A photothermal-response oxygen release platform based on a hydrogel for accelerating wound healing

Chunyang Li[1], Xiaojun He[2], Qingfeng Li[3], Mingzhi Lv[1], Jianliang Shen[2,4], Lin Jin[3] and Deyan He[1]

Abstract

During wound healing, oxygen availability and the anti-inflammatory microenvironment play an important role in the formation of new tissue. However, providing continuous and controllable oxygen around the injured tissue while inhibiting inflammation and realizing the synergistic effect of oxygen supply and anti-inflammation is still a major problem affecting the regeneration and repair of wound tissue. Inspired by skin wound pathology and the inflammatory microenvironment, a photothermal response-assisted strategy was developed in this study. We prepared a composite hydrogel system of polydopamine-hyaluronic acid (PDA-HA) hydrogel-loaded calcium peroxide-indocyanine green combined with lauric acid and manganese dioxide (CaO_2-ICG@LA@MnO_2) nanoparticles that showed excellent photothermal performance under near-infrared (NIR) irradiation and realized the on-off release of oxygen and reactive oxygen species (ROS). Controllable and sustainable oxygen release can promote the regeneration and repair of damaged tissue, and the generated ROS can effectively inhibit the outbreak of inflammation at the initial stage of wound healing. We believe that the system we have developed can be used in a new approach for treating chronic wounds.

Introduction

Wound repair is one of the most complex biological processes in humans[1,2]. Many studies have shown that sufficient oxygen is essential for proper wound healing[3–6]. However, the environment around wounds is highly hypoxic during wound healing for the following reasons: (I) In addition to the normal consumption of O_2 during aerobic respiration to meet the basic energy requirements, O_2 is also consumed through the generation of new vessels and connective tissue, the production of reactive oxygen species (ROS), and the action of NADPH oxidase in phagocytes[3,5]. (II) Adequate O_2 supply may be prevented due to disruption of the microcirculation and contraction of the vessels in traumatized tissue[5]. (III) Wound dressings may prevent wound tissues from receiving oxygen from the air. Therefore, it is a considerable challenge to design materials that can provide prolonged and sufficient oxygen to hypoxic regions[7,8].

Nanomaterials and nanotechnologies are expected to provide innovative platforms for tissue repair and regeneration[9–12]. Among a large number of oxygen-releasing materials, calcium peroxide (CaO_2), which decomposes in water to produce O_2, is preferred due to its high oxygen-generation capacity[13,14], while manganese dioxide (MnO_2) can improve the oxygenation rate as a catalyst. In particular, CaO_2 composite nanomaterials have been widely applied in tissue engineering[15–19]. However, the application of these materials has been greatly limited by the burst release of O_2, which not only leads to oxidative damage to cells[8] but also significantly reduces the continuous supply of O_2. Therefore, recent studies have focused on the design of oxygen-releasing materials for controlled O_2 production[16–20]. CaO_2 nanomaterials, because of their small size, can be easily coated, and the

Correspondence: Lin Jin (jinlin_1982@126.com) or Deyan He (hedy@lzu.edu.cn)
[1]School of Materials & Energy, Lanzhou University, 730000 Lanzhou, China
[2]School of Ophthalmology & Optometry, School of Biomedical Engineering, Wenzhou Medical University, 325035 Wenzhou, China
Full list of author information is available at the end of the article

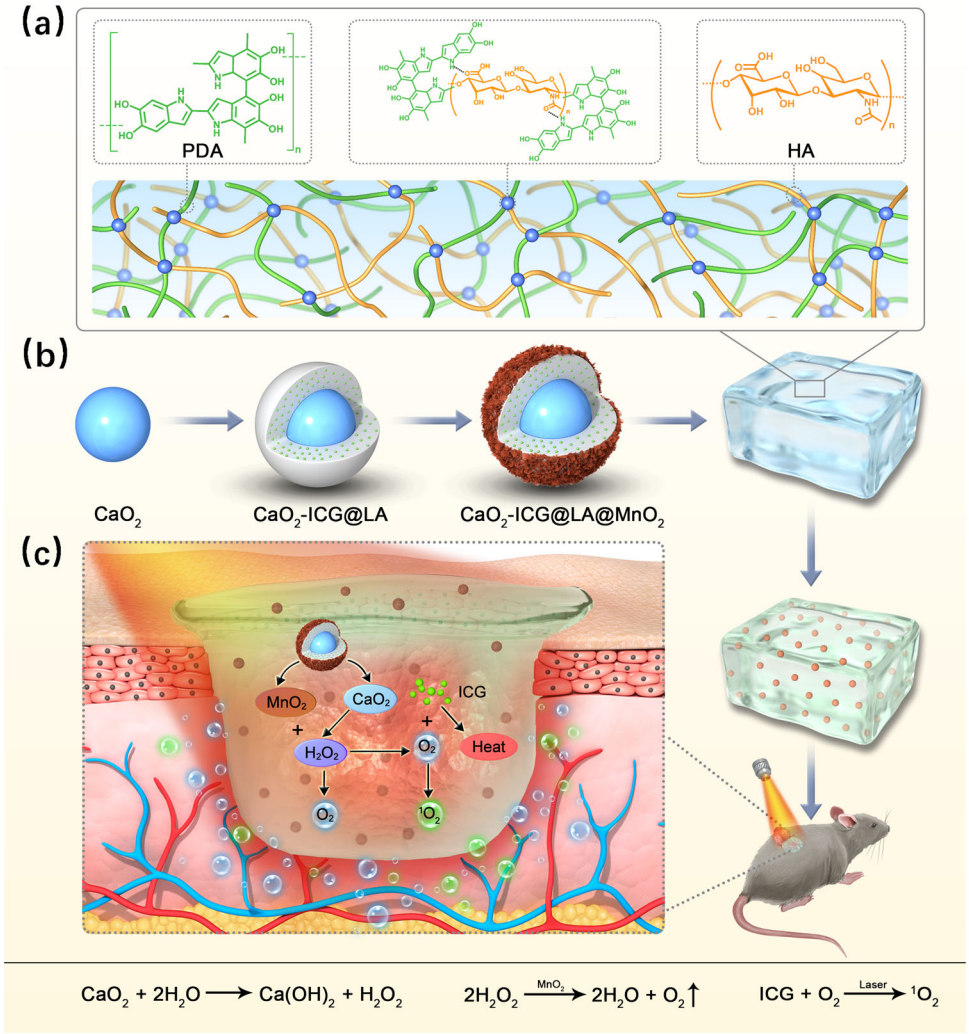

Scheme 1 Schematic illustration of the preparation and application of the nanocomposite hydrogel. **a** Synthesis of the PDA-HA hydrogel. **b** Preparation of CaO_2 nanocomposite particles. **c** Applications of the nanocomposite hydrogel in wound healing.

coatings can prevent exposure to an aqueous environment by providing a response to stimuli such as temperature, near-infrared (NIR) irradiation or pH. Thus, controlled release of O_2 can be realized by regulating the coatings. Indocyanine green (ICG), which is responsive to NIR light[21,22], has been used to coat CaO_2 nanoparticles to realize the controlled release of O_2. Under NIR irradiation, ICG releases singlet oxygen ($^1O_2$), a type of ROS[16,23,24]. $^1O_2$ is known to be highly reactive and can effectively damage DNA, proteins, and lipids[25,26]. Therefore, it can also have a positive effect on wound healing in the initial stage of inflammation. On the other hand, as a scaffold material, hydrogel is often used as a wound patch, which can adhere to wounds and release drugs, accelerate wound healing, and provide enough volume to encapsulate these oxygen-releasing materials[27–31], and the structure is conductive to oxygen transport[32].

Herein, we designed CaO_2-ICG@LA@MnO_2 composite nanoparticles with a good NIR response based on well-dispersed CaO_2 nanoparticles. The obtained CaO_2-ICG@LA@MnO_2 nanoparticles were further encapsulated in a PDA-HA hydrogel. Lauric acid (LA) causes swelling under NIR laser irradiation due to its low melting point (44 °C) and the photothermal property of ICG. Then, O_2 is generated as CaO_2 is exposed to an aqueous environment. We achieved the controlled release of O_2, and then a full-thickness skin defect repair test was carried out in rats with the prepared oxygen-releasing material. The in vivo experiments showed that the strategy effectively promoted wound healing by inducing a synergistic effect of O_2 supply and anti-inflammation in the microenvironment through the NIR response (Scheme 1).

Materials and methods

Materials

Calcium chloride dihydrate ($CaCl_2$, ACS, ≥99%), ammonia solution (AR, 25–28%), hydrogen peroxide solution (ACS, 30 wt. % in H_2O), and lauric acid (LA, GR, 99%) were purchased from Shanghai Aladdin Biochemical Technology Co., Ltd. Dopamine hydrochloride (DA, 98%), hyaluronic acid (HA, 97%), indocyanine green (ICG, 75%) and ammonium persulfate (AP, AR, 98.5%) were purchased from Shanghai Macklin Biochemical Co., Ltd. α-MnO_2 superfine powder was purchased from Jiangsu Xiamen Nanomaterial Technology Co., Ltd. Singlet oxygen sensor green (SOSG) was purchased from Thermo Fisher Scientific (China) Co., Ltd. All other chemicals and reagents were analytical grade and purchased from commercial sources unless otherwise stated.

Synthesis of CaO_2 nanoparticles

CaO_2 nanoparticles were synthesized at room temperature according to a previous report[13]. First, a 2 mol L^{-1} $CaCl_2$ aqueous solution was prepared as the original solution. Second, 1 mL of $CaCl_2$ solution was added to 60 mL of methanol, and 1 mL of hydrogen peroxide was mixed into the solution. After a few minutes, 4 mL of ammonia solution was dropped into the mixed solution to initiate the reaction. Finally, the product was separated by centrifugation, washed with ethanol three times at 5000 *rpm* for 5 min, and dried in a vacuum oven at ~60 °C for 12 h. Thus, the CaO_2 nanoparticles were successfully fabricated. The samples were measured by X-ray diffraction (XRD) using an X-ray diffractometer (D8 Focus Advance, Bruker) with Cu Kα radiation ($\lambda = 0.15406$ nm). Transmission electron microscopy (TEM) and high-resolution TEM (HR-TEM) images of the samples were obtained using a transmission electron microscope (JEM 2100 F, JEOL) at an accelerating voltage of 200 kV equipped with an energy-dispersive X-ray spectrometer (EDX, X-max 80 T, Oxford).

Fabrication of CaO_2-ICG@LA nanoparticles

First, 25 mg of CaO_2 was mixed into 25 mL of methanol, and the mixed solution was stirred for 20 min after 30 min of ultrasonic treatment. Second, 5 mg of ICG was dispersed in the mixed solution and stirred for 20 min, and then 1 g of LA was added, and the solution was stirred for 6 h. Finally, the product was separated by centrifugation, washed with methanol twice at 10000 *rpm* for 10 min, and dried at room temperature. Thus, CaO_2-ICG@LA nanoparticles were successfully fabricated. The morphology of the CaO_2-ICG@LA nanoparticles was observed with TEM.

Synthesis of CaO_2-ICG@LA@MnO_2 nanoparticles

MnO_2 nanoparticles (5 mg) were mixed into 20 mL of ethanol with ultrasonic treatment for 60 min, and then 10 mg of CaO_2-ICG@LA nanoparticles was added. A mixed solution of CaO_2-ICG@LA@MnO_2 was obtained, and CaO_2-ICG@LA@MnO_2 nanoparticles were prepared by drying the mixed solution at room temperature. The morphology and element composition of the samples were analyzed by TEM and EDX.

Measurement of O_2 concentration

While vigorously stirring at room temperature, 3 mL of CaO_2, 3 mL of CaO_2-ICG@LA, or 3 mL of CaO_2-ICG@LA@MnO_2 methanol solution (0.5 mg mL^{-1}) was added to 27 mL of phosphate-buffered saline (PBS, 10 mM, pH 7.4). Then, the O_2 concentration in the solution was recorded in real time with a dissolved oxygen meter (JPSJ-605F, Shanghai Leici Scientific Instrument Co., Ltd.).

Fabrication of the hydrogels

DA and HA were used to fabricate the biomimetic PDA-HA hydrogel. Briefly, 0.125 g of DA was dissolved in 2.5 mL of PBS. Minutes later, 125 μL aqueous solution of AP (0.02 g mL^{-1}) was added to the solution. Then, 0.2 g HA was added to the mixture with vigorous stirring for ~5 min. Finally, the PDA-HA hydrogel was fabricated. Hereby, the nanocomposite (NC) hydrogel was prepared by replacing 2.5 mL of PBS with 2.0 mL of PBS and 0.5 mL of CaO_2-ICG@LA@MnO_2 methanol solution (1.0 mg mL^{-1}). Here, the CaO_2-ICG@LA@MnO_2 methanol solution was prepared by mixing 20 mg CaO_2-ICG@LA@MnO_2 and 5 mg ICG into 20 mL of methanol. The microstructures of the obtained DA-HA hydrogel were investigated by scanning electron microscopy (SEM, Quanta 200, FEI). The freeze-dried samples were coated with gold before observation. The accelerating voltage was 25 kV.

Photothermal performance of the hydrogel

To evaluate the NIR photothermal performance of the PDA-HA hydrogel, the as-prepared hydrogel with a mass of 1.0 g was cut into cubes (15 mm × 15 mm × 4 mm) and then exposed to an 808 nm NIR laser (MW-GX-808/1~5000 mW, Changchun Laser Optoelectronics Technology Co., Ltd.). The hydrogel temperature was monitored as a function of irradiation time.

Measurement of $^1O_2$ generation

SOSG is a highly selective reagent for detecting $^1O_2$. In the presence of $^1O_2$, it emits a green fluorescence similar to fluorescein. To observe this, first, SOSG was diluted to 500 μM using methanol as the solvate, and 45 μL of SOSG solution was added to the NC hydrogel. Then, 1.0 g of NC hydrogel and 2.0 mL of PBS solution were added to a sample cell, and the photoluminescence (PL) intensity of the sample was monitored under NIR (808 nm) laser irradiation. PL spectra were obtained by a PL spectrometer (FLS920P, Edinburgh) using a 450 W Xenon lamp as an excitation source.

Wound healing in a full-thickness skin defect model

A rat full-thickness wound model was used to evaluate the effect of the CaO_2-ICG@LA@MnO_2 composite hydrogel on wound healing. Rats were randomly divided into 3 groups with 5 rats in each group, which included Group I (control), Group II (NC hydrogel), and Group III (NC hydrogel + NIR). Their backs were shaved, and a rounded full-thickness cutaneous wound was created with a diameter of 8 mm. In Group I, the wounds were treated with 200 μL PBS only. In Groups II and III, the wounds were covered with the NC hydrogel. In Group III, the wounds were irradiated by an NIR laser for 3 min once a day. The recovery of the wounds was evaluated on Days 0, 3, 5, 10, and 14.

Histological and immunofluorescence analysis

The wound tissues were collected on Day 14. The specimens were fixed with 4% paraformaldehyde, embedded in paraffin, and cut into 5 μm thick sections. The histological sections were stained with hematoxylin and eosin (H&E) and Masson trichrome stains after deparaffinization and rehydration. In addition, the main organs (heart, liver, spleen, lung, and kidney) were collected for histological analysis by H&E staining. For immunofluorescence staining, tissue sections were deparaffinized, rehydrated, and subjected to thermally induced antigen retrieval in citrate buffer solution (10 mM, pH 6.0) at 98 °C for 10 min. Then, 10% normal goat serum was employed to block nonspecific binding for 70 min. TNF-α and TGF-β primary antibodies and corresponding secondary antibodies were used to evaluate the phenotype of macrophages in wound tissue. The cell nuclei were counterstained with DAPI for 10 min. The H&E- or Masson-stained sections were observed by an optical microscope. Immunofluorescence images were obtained by a fluorescence microscope (Olympus, Japan) and analyzed by ImageJ software.

Live subject statement

Eight-week-old rats were collected from Wenzhou Medical University. Animal experiments were performed according to the protocols approved by the Animal Ethics Committee of Wenzhou Medical University (No. SYXK-2021-0020).

Results

The preparation of CaO_2-ICG@LA@MnO_2 nanoparticles was based on the as-synthesized CaO_2 nanomaterials. The CaO_2 nanoparticles were synthesized according to a previous report[13], as described in the experimental section. A TEM image of the CaO_2 nanoparticles is shown in Fig. 1a. Clearly, the well-dispersed CaO_2 nanoparticles exhibit irregular morphology, and the particle sizes are mainly in the range of 50–150 nm. As shown in Fig. 1b, the typical HR-TEM image of CaO_2 nanoparticles clearly shows the (002) and (110) planes

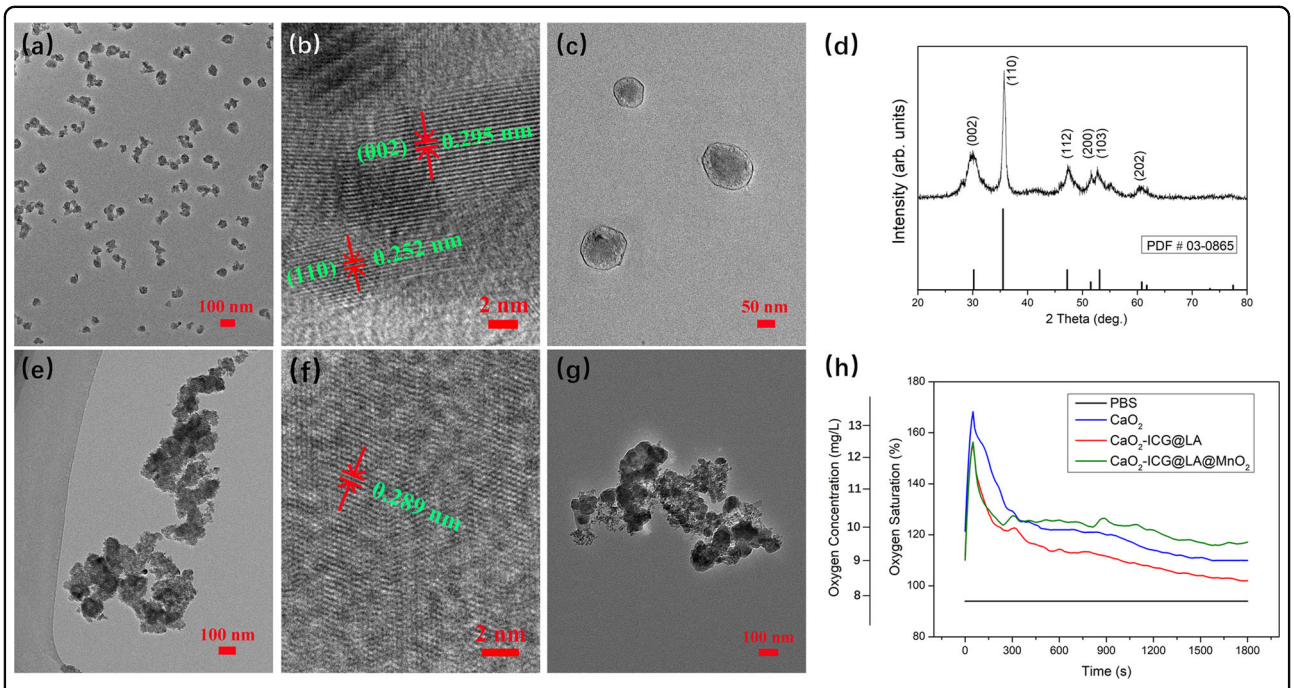

Fig. 1 Morphologies, structures, and the oxygen-producing capacities of the oxygen-releasing nanoparticles. a TEM and (**b**) HR-TEM images of CaO_2 nanoparticles. **c** TEM image of CaO_2-ICG@LA nanoparticles. **d** XRD image of CaO_2 nanoparticles. **e** TEM and (**f**) HR-TEM images of MnO_2 nanoparticles. **g** TEM image of CaO_2-ICG@LA@MnO_2 nanoparticles. **h** O_2 concentration measurement in PBS.

with corresponding lattice spacings of 0.295 and 0.252 nm, respectively. Figure 1d shows the XRD images of the as-prepared CaO_2 nanoparticles. All diffraction peaks of the samples were readily indexed to the standard card of tetragonal CaO_2 (PDF#03-0865). The results indicate that the prepared CaO_2 nanoparticles have a tetragonal structure with cell constants of a = 0.354 nm, b = 0.354 nm and c = 0.591 nm. Subsequently, CaO_2-ICG@LA nanoparticles were synthesized, and their morphologies were observed by TEM. As shown in Fig. 1c, CaO_2-ICG@LA nanoparticles have a core-shell structure, in which CaO_2 nanoparticles are wrapped by LA. A certain amount of ICG exists on the surface of CaO_2 and inside of LA. Next, CaO_2-ICG@LA@MnO_2 nanoparticles were obtained by the simple method described in the experimental section. The α-MnO_2 nanoparticles used were purchased from Jiangsu Xianfeng Nanomaterial Technology Co., Ltd., and their TEM image is shown in Fig. 1e. The MnO_2 nanoparticles have a texture like the fluffy surface of a towel, and larger nanoparticles are ~100 nm in size. The HR-TEM image (Fig. 1f) shows that the interplanar distance of the nanoparticles is ~0.289 nm, which is consistent with previous reports[33,34]. TEM images of the CaO_2-ICG@LA@MnO_2 nanoparticles are shown in Fig. 1g. It is evident that there are CaO_2-ICG@LA and α-MnO_2 structures in this material. The chemical element distributions of the CaO_2-ICG@LA@MnO_2 nanoparticles were further studied by EDX element mapping analysis techniques, as shown in Fig. S1. Considering that the nanoparticles contain more elements, several typical elements were detected, such as Ca, Mn, O, S and N. As mentioned above, it is very important to build a controllable oxygen release system. As an oxygen release material, CaO_2 has attracted considerable attention due to its high oxygen generation capacity and the biocompatibility of calcium ions. In addition, MnO_2 is used as a catalyst in this reaction. The mechanism of oxygen generation is described by the following chemical equations.

$$CaO_2 + 2H_2O \rightarrow Ca(OH)_2 + H_2O_2 \quad (1)$$

$$2H_2O_2 \overset{MnO_2}{\rightarrow} 2H_2O + O_2 \uparrow \quad (2)$$

In the aqueous environment, CaO_2 is hydrolyzed to H_2O_2 and then to O_2. By limiting the exposure of CaO_2 to water

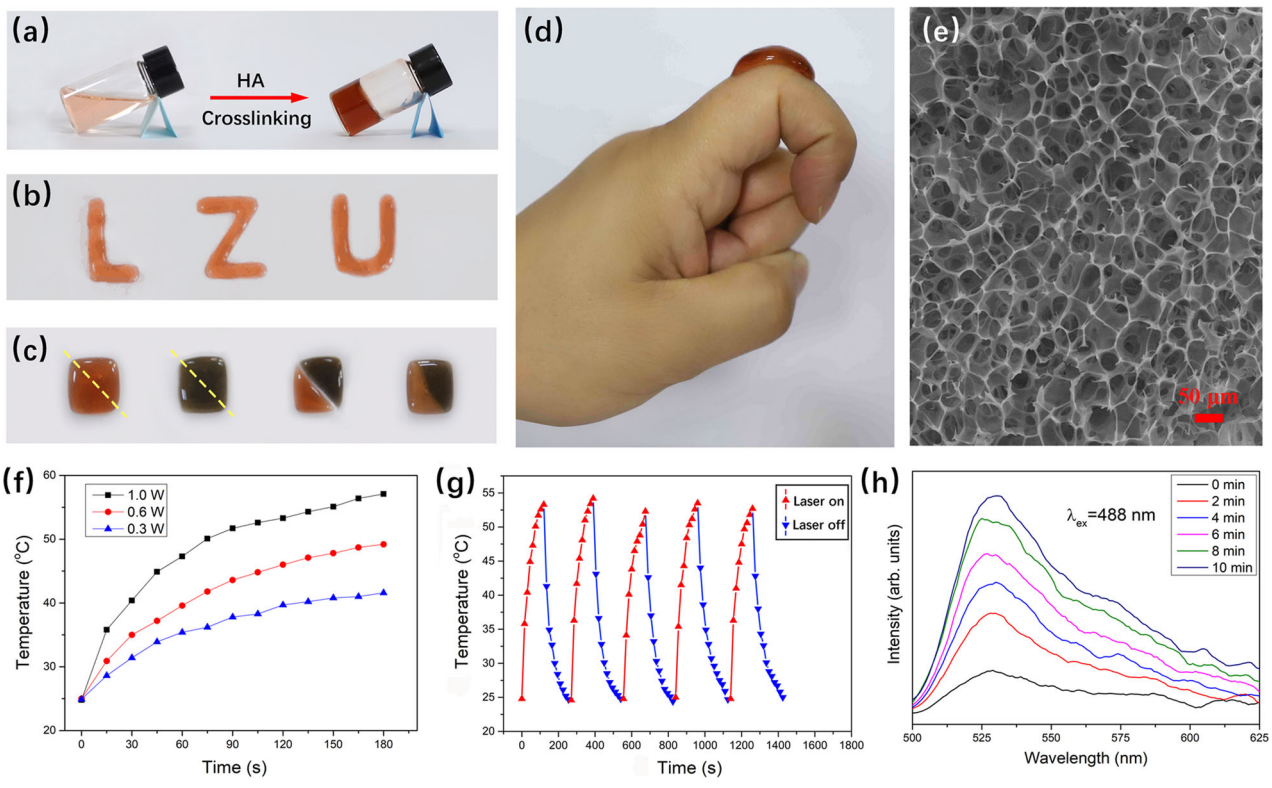

Fig. 2 Fabrication, morphology, and properties of PDA-HA hydrogel. a Gelation process, (**b**) reformability, (**c**) self-healing, (**d**) bioadhesion, and (**e**) SEM image of the PDA-HA hydrogel. **f** Photothermal-heating curves of the PDA-HA hydrogel under 808 nm laser irradiation (0.3, 0.5 or 1.0 W cm^{-2}) for 3 min. **g** Heating curves of the PDA-HA hydrogel for 5 on-off cycles under 808 nm laser irradiation (1.0 W cm^{-2}). **h** PL emission spectra of the PDA-HA hydrogel in PBS solution with λ_{ex} = 488 nm.

molecules, we can control oxygen generation. Here, due to the hydrophobicity and low melting point of LA, it was chosen to coat the CaO_2 nanoparticles. CaO_2, CaO_2-ICG@LA and CaO_2-ICG@LA@MnO_2 nanoparticles were mixed into PBS solution, and the dissolved oxygen in the solution was measured, as shown in Fig. 1h. Due to the complete exposure to water molecules, CaO_2 nanoparticles generated more oxygen in the first 300 s than the CaO_2-ICG@LA and CaO_2-ICG@LA@MnO_2 nanoparticles. LA-coated CaO_2-ICG@LA nanoparticles generate less oxygen, while CaO_2-ICG@LA@MnO_2 nanoparticles release more oxygen under the catalysis of MnO_2. Moreover, after continuous oxygen generation for 30 min, the release of oxygen from CaO_2-ICG@LA@MnO_2 nanoparticles was further monitored in the range of 25–50 °C, as shown in Fig. S2. Below 40 °C, the amount of oxygen released increases with temperature, mainly due to dissolved oxygen in PBS. Above 40 °C, oxygen production is significantly improved because of the melting of LA.

The physicochemical properties of the synthesized PDA-HA[35–37] and NC hydrogels were investigated. The gelation process is shown in Fig. 2a. DA was dissolved in PBS, and then a certain amount of AP aqueous solution was added as an oxidant to induce dopamine polymerization. The mixture turned a clear pale red after stirring for a few minutes. Then, HA was added to the mixture and stirred vigorously for ~5 min to prepare the firebrick PDA-HA hydrogel (Fig. 2a). The hydrogel has a double-network structure and overcomes the problem of brittleness. In addition, the short gelation time is beneficial to the application of the PDA-HA hydrogel in wound healing. The PDA-HA hydrogel is flexible enough to construct any shape, as shown in Fig. 2b. It is well known that hydrogels with self-healing properties can greatly improve the lifespan of dressings, and the self-healing capability of the PDA-HA hydrogel was further evaluated. In Fig. 2c, a simple self-healing process of the hydrogel is shown. We cut two squares at the same position and patched two pieces of different hydrogels into a new square, one of which was stained with ICG. Self-healing was achieved 5 min after physical contact. Simultaneously, the hydrogel exhibited excellent bioadhesion performance on the skin, as shown in Fig. 2d. In addition, the microstructure of the hydrogel was observed by SEM. It can be seen from Fig. 2e that the hydrogel is porous with an average pore size of ~42 μm.

Hydrogels are a fascinating platform for use as three-dimensional (3D) scaffolds for tissue repair and delivery of therapeutic molecules and cells[38]. The physicochemical and biological properties of hydrogels can be enhanced by combining them with bioactive and functional nanomaterials. NC hydrogels with ICG photothermal properties were obtained by introducing ICG into PDA-HA hydrogels. It is well known that ICG is a photothermal agent that absorbs NIR light (~800 nm). In addition, it is an NIR clinical imaging agent that has been approved by the U.S. Food and Drug Administration[21,22]. Photothermal therapy is based on the photothermal effect and has been applied to clinical treatment[39–41]. Therefore, the photothermal properties of the NC hydrogel were investigated. Under irradiation with an 808 nm NIR laser with different power densities (0.3, 0.5 and 1.0 Wcm^{-2}), it was found that the

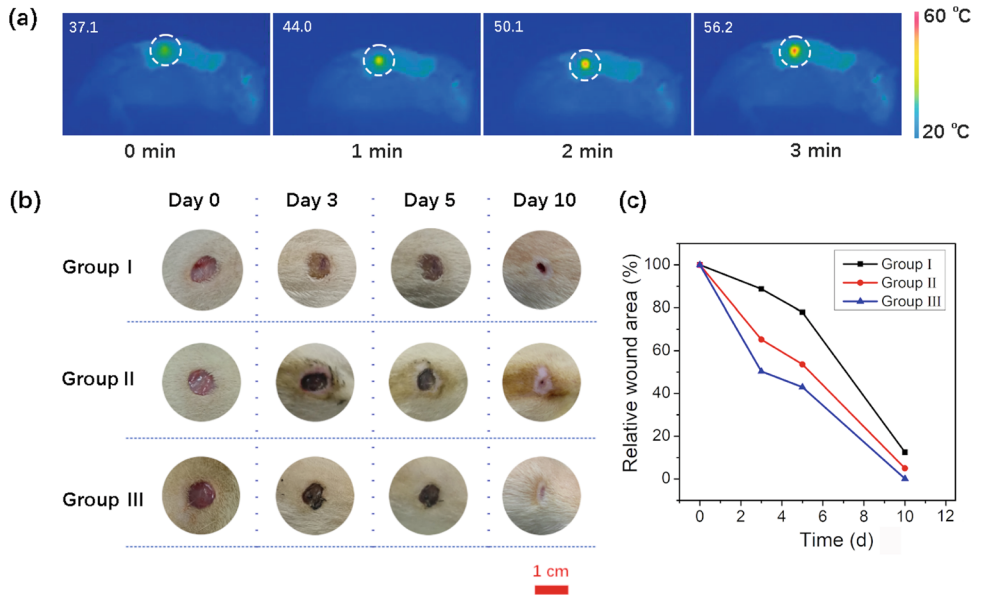

Fig. 3 Evaluation of wound closure with NC hygrogel. a Photothermal images of a rat treated with NC hydrogel under NIR irradiation (808 nm, 1.0 W cm^{-2}) for 0–3 min. **b** Representative images of skin wounds treated with PBS (Group I), NC hydrogel (Group II), and NC hydrogel + NIR (Group III). **c** Relative wound area curves of rats after different treatments.

temperature of the hydrogel increases with increasing laser irradiation time and power density, as shown in Fig. 2f. The photothermal stability of the NC hydrogel under repeated NIR laser irradiation was further investigated, and the heating (laser on) and cooling (laser off) processes for 5 cycles are shown in Fig. 2g. The heating profiles are similar for all cycles, with no significant change during the cycles. ICG generates $^1O_2$ under 808 nm laser irradiation[16,24]. With the in-depth study of $^1O_2$, an increasing number of important applications have been found, such as photodynamic therapy, sterilization, and blood pressure regulation[22,25,42]. Wound healing involves four overlapping stages, namely, hemostasis, inflammation, proliferation and remodeling, in which inflammation occurs throughout the whole process of wound healing. ICG can effectively inhibit the outbreak of inflammation at the initial stage of wound healing. SOSG is currently the most widely used $^1O_2$ probe and is detected by monitoring its PL at 528 nm[43,44]. In general, with proper control, the intensity of the green fluorescence signal can be correlated with the $^1O_2$ concentration. As shown in Fig. 2h, the increase in PL intensity confirms that the $^1O_2$ concentration increases with time.

To investigate the promoting effect of the hydrogel on wound healing, a full-thickness skin defect repair experiment was conducted in rats. The rats were randomly divided into 3 groups with 5 rats in each group, which included Group I (control), Group II (NC hydrogel), and Group III (NC hydrogel + NIR). A rounded full-thickness cutaneous wound was created on their backs and monitored over time. The rats in in Group III had their wounds treated with NC hydrogel and were irradiated by an 808 nm laser (1.0 W cm^{-2}), and photothermal images were recorded by an infrared thermal imaging camera from 0 to 3 min (Fig. 3a). On Day 10, the rats in Group III exhibited the best wound healing, in which the wounds were completely closed. Wounds were not fully closed in Groups I and II (Fig. 3b). Moreover, the wound healing rate curve also demonstrated that the wound healing of rats in Group III was faster than that in the other groups (Fig. 3c). After 3 d of treatment, the wound area of Group III (NC hydrogel + NIR) was reduced to nearly 50% of its original size, while 89% remained for Group I (control group) and 65% for Group II (NC hydrogel). As shown in Fig. 3b, Group I required 7.1 d for half of the wound to be recovered, while Group II required 5.2 d. In addition, considerable redness

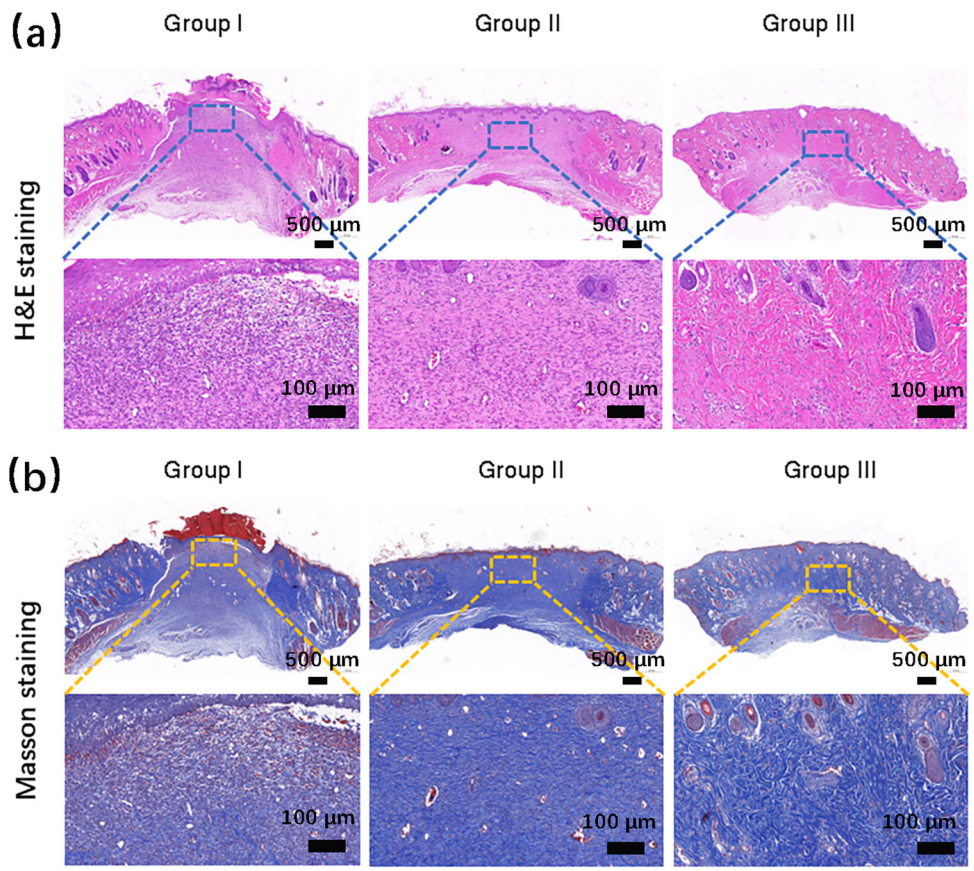

Fig. 4 Evaluation of wound healing with NC hydrogle. a H&E and (**b**) Masson staining of wounds on Day 14.

and swelling were observed in Group II after 3 d of treatment. Inflammation is a basic pathological process dominated by the defense response when biological tissues are exposed to certain stimuli, including trauma, infection and other damaging factors. Local manifestations of inflammation include redness, swelling, fever, pain, dysfunction, and systemic reactions such as fever and changes in peripheral blood leukocyte counts. The redness and swelling in Group II were attributed to the stimulation of the hydrogel coating, while those symptoms were not observed in Group III due to the presence of $^1O_2$ and photothermal effects. On Day 5, the redness and swelling of Group II gradually reduced. In addition, the wound healing rates of Group II and Group III became slow on the surface, which could be related to the internal healing of the wounds. On Day 10, based on external observations, the wounds of Group III were completely closed, with small scars surrounded by normal fur tissue. The wounds of Group II were small with white patches and no surrounding hair, which was attributed to hydrogel shedding. Notably, after 10 d, more than 99% of the total area healed in Group III, and ~13% and 5% of wound tissue remained in Group I and Group II, respectively.

Moreover, H&E staining and Masson staining were performed to further analyze the wound repair process from a histological perspective. As shown in Fig. 4, fully closed wounds were formed in all 3 groups, but wound closure in Groups II and III was better than that in Group I. Masson staining mainly reflects the generation of collagen fibers, and a larger blue area represents more collagen fibers, indicating that the effect of repair is better. It was clear that better tissue structures were formed in Group III than in the other groups. All H&E staining (Fig. 4a) and Masson staining (Fig. 4b) showed that the treatment given to Group III (NC hydrogel + NIR irradiation) leads to better wound closure and has a better therapeutic effect on full-thickness skin incisions.

Immunofluorescence analysis was conducted according to the changes in proinflammatory and anti-inflammatory

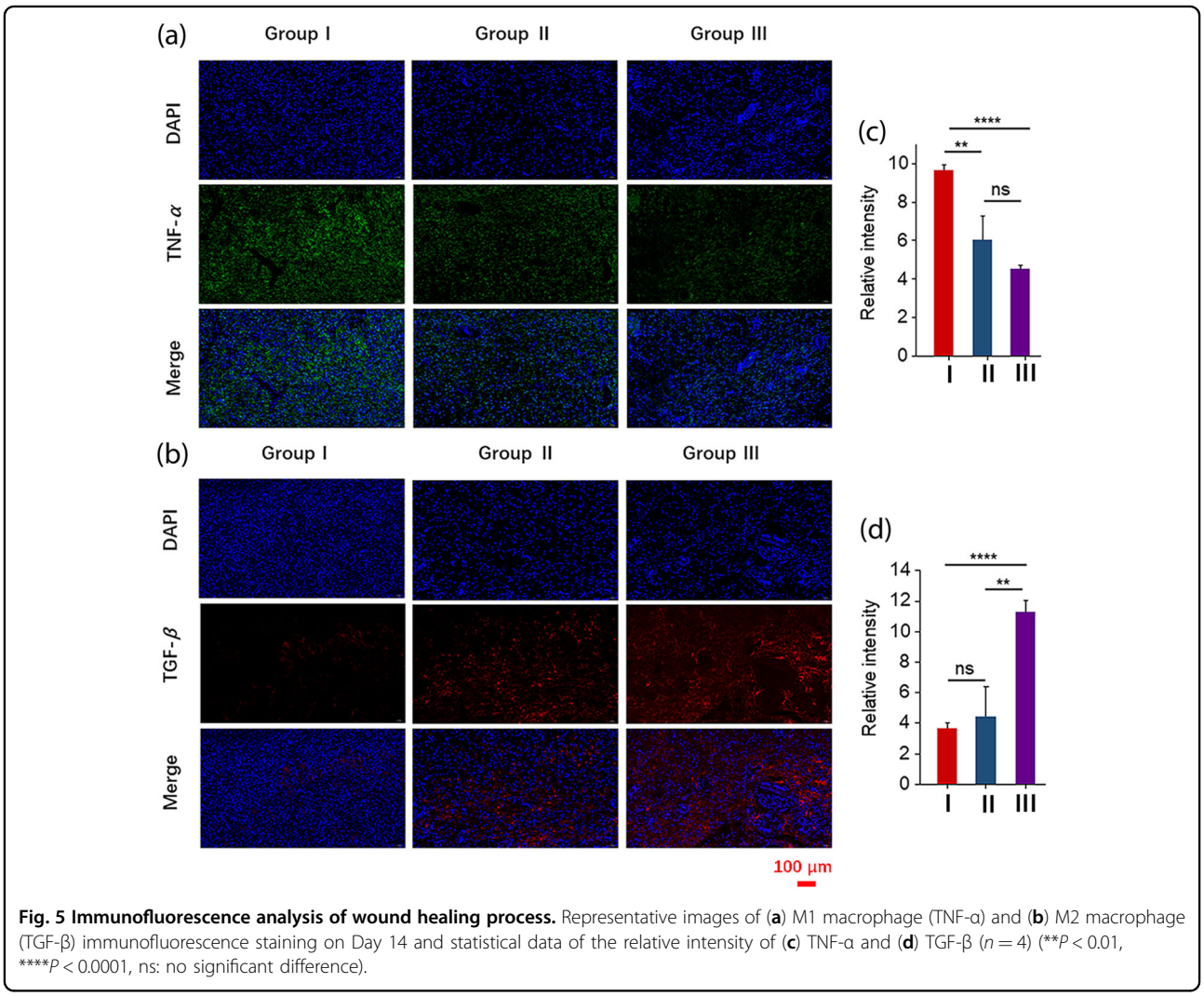

Fig. 5 Immunofluorescence analysis of wound healing process. Representative images of (**a**) M1 macrophage (TNF-α) and (**b**) M2 macrophage (TGF-β) immunofluorescence staining on Day 14 and statistical data of the relative intensity of (**c**) TNF-α and (**d**) TGF-β ($n = 4$) (**$P < 0.01$, ****$P < 0.0001$, ns: no significant difference).

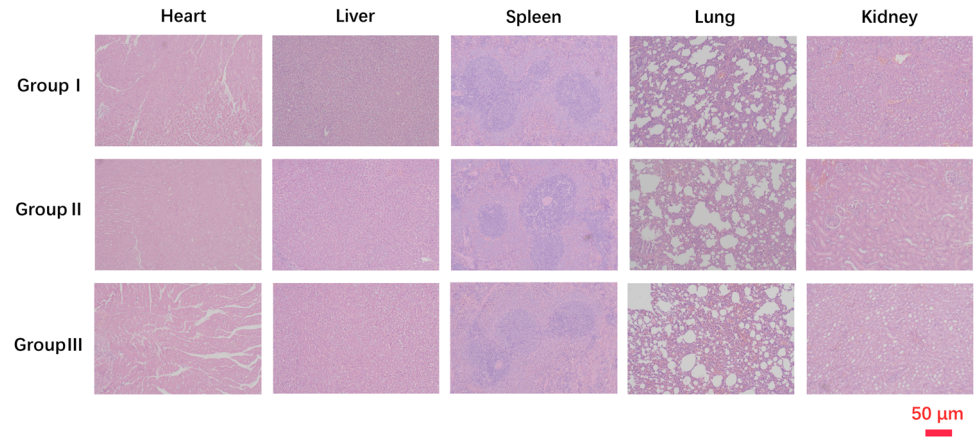

Fig. 6 In vivo biocompatibility of NC hydrogel. H&E staining of major organs (heart, liver, spleen, lung and kidney) of the rats after different treatments on Day 14.

macrophages during wound recovery. As mentioned above, inflammation is present throughout the wound healing process. Therefore, changes in wound inflammation in rats were observed by tissue immunofluorescence staining. In the process of wound healing, there are two types of macrophages, proinflammatory (M1) and anti-inflammatory (M2) macrophages[45,46], whose markers change to a certain extent. Wound inflammation can be assessed indirectly by investigating corresponding markers in tissues. Hence, immunofluorescence staining of macrophages was performed on wound sections during the proliferation phase (Day 14) to clarify the role of the NC hydrogel in the conversion of M1 macrophages into the M2 phenotype. As shown in Fig. 5a, b, NC hydrogel + NIR treatment reduced the proportion of TNF-α M1-labeled positive cells, and the infiltration and distribution of TGF-β M2-labeled positive cells were enhanced compared with other groups. These results can be further observed in Fig. 5c, d, which show statistical data of the relative intensity of TNF-α (c) and TGF-β (d), respectively. M2 macrophages secrete anti-inflammatory mediators during wound healing, and our results further confirm that NC hydrogel + NIR can increase the presence of the macrophage phenotype relevant to tissue healing and regeneration.

To determine the biosafety and side effects of the NC hydrogel, H&E-stained slices of major organs such as the heart, liver, spleen, lung, and kidney were evaluated after 14 days of treatment (Fig. 6). The results showed no apparent histological abnormalities or lesions, confirming the biosafety of the NC hydrogel in living organisms[17,47,48].

Conclusions

Well-dispersed CaO_2 nanoparticles were synthesized, and their morphology and structure were characterized by TEM and XRD. CaO_2-ICG@LA@MnO_2 composite nanoparticles were constructed by using CaO_2 nanoparticles, and their oxygen release could be efficiently regulated by LA. Furthermore, NC hydrogels with photothermal properties were designed to achieve continuous release of oxygen upon 808 nm laser irradiation. The control group, hydrogel group, and hydrogel (laser irradiation) group were subjected to a full-thickness skin defect repair test in rats, and the hydrogel (laser irradiation) group had the most effective wound healing. This was further confirmed by H&E staining, Masson staining, and immunofluorescence analysis.

Acknowledgements

This work was supported by the National Natural Science Foundation of China (11674138), the Program for Innovative Research Team (in Science and Technology) at the University of Henan Province (23IRTSTHN008), the Science and Technology Research Project of Henan Province (212102210034), and the Key Technologies R & D Program of Henan Province (No. 222102240100).

Author details

[1]School of Materials & Energy, Lanzhou University, 730000 Lanzhou, China. [2]School of Ophthalmology & Optometry, School of Biomedical Engineering, Wenzhou Medical University, 325035 Wenzhou, China. [3]Henan International Joint Laboratory of Biomedical Nanomaterials, Zhoukou Normal University, 466001 Zhoukou, China. [4]Wenzhou Institute, University of Chinese Academy of Sciences, 325000 Wenzhou, China

Author contributions

C.Y.L. conducted the experiments and wrote the original draft. X.J.H. and Q.F.L. performed the data analyses. M.Z.L. investigated and visualized the data. J.L.S. and L.J. contributed to discussion and interpretation of the results. D.Y.H. finalized the paper and supervised the project.

Competing interests

The authors declare no competing interests.

Supplementary information The online version contains supplementary material available at https://doi.org/10.1038/s41427-022-00456-7.

Received: 27 August 2022 Revised: 26 November 2022 Accepted: 30 November 2022.
Published online: 13 January 2023

References

1. Gurtner, G. C., Werner, S., Barrandon, Y. & Longaker, M. T. Wound Repair and Regeneration. *Nature* **453**, 314–321 (2008).
2. Eming, S. A., Martin, P. & Tomic-Canic, M. Wound Repair and Regeneration: Mechanisms, Signaling, and Translation. *Sci. Transl. Med.* **6**, 265sr6 (2014).
3. Schreml, S. et al. Oxygen in Acute and Chronic Wound Healing. *Brit. J. Dermatol.* **163**, 257–268 (2010).
4. Castilla, D. M., Liu, Z. J. & Velazquez, O. C. Oxygen: Implications for Wound Healing. *Adv. Wound Care* **1**, 225–230 (2011).
5. Gottrup, F. et al. Use of Oxygen Therapies in Wound Healing. *J. Wound Care* **26**, S1–S43 (2017).
6. Chen, H. H. et al. Dissolved Oxygen from Microalgae-Gel Patch Promotes Chronic Wound Healing in Diabetes. *Sci. Adv.* **6**, eaba4311 (2020).
7. Guan, Y. et al. Sustained Oxygenation Accelerates Diabetic Wound Healing by Promoting Epithelialization and Angiogenesis and Decreasing Inflammation. *Sci. Adv.* **7**, eabj0153 (2021).
8. Shiekh, P. A., Singh, A. & Kumar, A. Oxygen Releasing Antioxidant Cryogel Scaffolds with Sustained Oxygen Delivery for Tissue Engineering Applications. *ACS Appl. Mater. Interfac.* **10**, 18458–18469 (2018).
9. Luo, Z. Q. et al. Microfluidic Electrospray Photo-Crosslinkable κ-Carrageenan Microparticles for Wound Healing. *Eng. Regeneration* **2**, 257–262 (2021).
10. Yu, Y. R., Wang, Q., Wang, C. & Shang, L. R. Living Materials for Regenerative Medicine. *Eng. Regeneration* **2**, 96–104 (2021).
11. Cai, L. J., Xu, D. Y., Chen, H. X., Wang, L. & Zhao, Y. J. Designing Bioactive Micro-/Nanomotors for Engineered Regeneration. *Eng. Regeneration* **2**, 109–115 (2021).
12. Furtado, M., Chen, L., Chen, Z. H., Chen, A. & Cui, W. G. Development of Fish Collagen in Tissue Regeneration and Drug Delivery. *Eng. Regeneration* **3**, 217–231 (2022).
13. Park, J. S., Song, Y. J., Lim, Y. G. & Park, K. Facile Fabrication of Oxygen-Releasing Tannylated Calcium Peroxide Nanoparticles. *Materials* **13**, 3864 (2020).
14. Cassidy, D. P. & Irvine, R. L. Use of Calcium Peroxide to Provide Oxygen for Contaminant Biodegradation in a Saturated Soil. *J. Hazard. Mater.* **B69**, 25–39 (1999).
15. Lv, X. G. et al. Structural and Functional Evaluation of Oxygenating Keratin/Silk Fibroin Scaffold and Initial Assessment of Their Potential for Urethral Tissue Engineering. *Biomaterials* **84**, 99–110 (2016).
16. Liu, C. H. et al. An Open Source and Reduce Expenditure ROS Generation Strategy for Chemodynamic/Photodynamic Synergistic Therapy. *Nat. Commun.* **11**, 1735 (2020).
17. Zhang, M. et al. Calcium-Overload-Mediated Tumor Therapy by Calcium Peroxide Nanoparticles. *Chem* **5**, 2171–2182 (2019).
18. Lu, Z. Y., Jiang, X., Chen, M. Q., Feng, L. & Kang, Y. J. An Oxygen-Releasing Device to Improve the Survival of Mesenchymal Stem Cells in Tissue Engineering. *Biofabrication* **11**, 045012 (2019).
19. Wu, D. et al. Efficacy-Shaping Nanomedicine by Loading Calcium Peroxide into Tumor Microenvironment-responsive Nanoparticles for the Antitumor Therapy of Prostate Cancer. *Theranostics* **10**, 9808–9829 (2020).
20. Razavi, M. et al. A Collagen Based Cryogel Bioscaffold that Generates Oxygen for Islet Transplantation. *Adv. Funct. Mater.* **30**, 1902463 (2020).
21. Shirata, C. et al. Near-Infrared Photothermal/Photodynamic Therapy with Indocyanine Green Induces Apoptosis of Hepatocellular Carcinoma Cells through Oxidative Stress. *Sci. Rep.* **7**, 13958 (2017).
22. Ma, Y., Tong, S., Bao, G., Gao, C. & Dai, Z. F. Indocyanine Green Loaded SPIO Nanoparticles with Phospholipid-PEG Coating for Dual-Modal Imaging and Photothermal Therapy. *Biomaterials* **34**, 7706–7714 (2013).
23. Sheng, G. P. et al. Encapsulation of Indocyanine Green into Cell Membrane Capsules for Photothermal Cancer Therapy. *Acta Biomater.* **43**, 251–261 (2016).
24. Sun, L. et al. Mesenchymal Stem Cells Functionalized Sonodynamic Treatment for Improving Therapeutic Efficacy and Compliance of Orthotopic Oral Cancer. *Adv. Mater.* **32**, 2005295 (2020).
25. Feng, Y., Sun, W. Z., Wang, X. S. & Zhou, Q. X. Selective Photoinactivation of Methicillin-Resistant Staphylococcus Aureus by Highly Positively Charged Ru^{II} Complexes. *Chem. Eur. J.* **25**, 1–7 (2019).
26. Sun, W. Z. et al. Fluorination in Enhancing Photoactivated Antibacterial Activity of Ru(II) Complexes with Photo-Labile Ligands. *RSC Adv.* **10**, 25364–25369 (2020).
27. Ouyang, J. et al. In Situ Sprayed NIR-Responsive, Analgesic Black Phosphorus-Based Gel for Diabetic Ulcer Treatment. *PNAS* **117**, 28667–28677 (2020).
28. Siebert, L. et al. Light-Controlled Growth Factors Release on Tetrapodal ZnO-Incorporated 3D-Printed Hydrogels for Developing Smart Wound Scaffold. *Adv. Funct. Mater.* **31**, 2007555 (2021).
29. Liu, Y. N. et al. Construction of Chitosan-Based Hydrogel Incorporated with Antimonene Nanosheets for Rapid Capture and Elimination of Bacteria. *Adv. Funct. Mater.* **30**, 2003196 (2020).
30. Li, C. D. & Cui, W. G. 3D Bioprinting of Cell-Laden Constructs for Regenerative Medicine. *Eng. Regeneration* **2**, 195–205 (2021).
31. Liu, C., Xu, X. Y., Cui, W. G. & Zhang, H. B. Metal-Organic Framework (MOF)-Based Biomaterials in Bone Tissue Engineering. *Eng. Regeneration* **2**, 105–108 (2021).
32. Liang, Y. Q., Li, Z. L., Huang, Y., Yu, R. & Guo, B. L. Dual-Dynamic-Bond Cross-Linked Antibacterial Adhesive Hydrogel Sealants with On-Demand Removability for Post-Wound-Closure and Infected Wound Healing. *ACS Nano* **15**, 7078–7093 (2021).
33. Ghosh, D., Bhandari, S. & Khastgir, D. Synthesis of MnO_2 Nanoparticles and Their Effective Utilization as UV Protectors for Outdoor High Voltage Polymeric Insulators Used in Power Transmission Lines. *Phys. Chem. Chem. Phys.* **18**, 32876–32890 (2016).
34. Wang, X. & Li, Y. D. Selected-Control Hydrothermal Synthesis of α- and β-MnO_2 Single Crystal Nanowires. *J. Am. Chem. Soc.* **124**, 2880–2881 (2002).
35. Huang, R. L. et al. Conjugation of Hyaluronic Acid onto Surfaces via the Interfacial Polymerization of Dopamine to Prevent Protein Adsorption. *Langmuir* **31**, 12061–12070 (2015).
36. Zhou, D. et al. Dopamine-Modified Hyaluronic Acid Hydrogel Adhesives with Fast-Forming and High Tissue Adhesion. *ACS Appl. Mater. Interfac.* **12**, 18225–18234 (2020).
37. Zou, C. Y. et al. Multi-Crosslinking Hydrogels with Robust Bio-Adhesion and Pro-Coagulant Activity for First-Aid Hemostasis and Infected Wound Healing. *Bioact. Mater.* **16**, 388–402 (2022).
38. Kurian, A. G., Singh, R. K., Patel, K. D., Lee, J.-H. & Kim, H.-W. Multifunctional GelMA Platforms with Nanomaterials for Advanced Tissue Therapeutics. *Bioact. Mater.* **8**, 267–295 (2022).
39. Zou, L. L. et al. Current Approaches of Photothermal Therapy in Treating Cancer Metastasis with Nanotherapeutics. *Theranostics* **6**, 762–772 (2016).
40. Zhao, P. H. et al. Local Generation of Hydrogen for Enhanced Photothermal Therapy. *Nat. Commun.* **9**, 4241 (2018).
41. Luo, H. H. et al. Light-Controlled Nanosystem with Size-Flexibility Improves Targeted Retention for Tumor Suppression. *Adv. Funct. Mater.* **31**, 2101262 (2021).
42. Stanley, C. P. et al. Singlet Molecular Oxygen Regulates Vascular Tone and Blood Pressure in Inflammation. *Nature* **566**, 548–552 (2019).
43. Lin, H. Y. et al. Feasibility Study on Quantitative Measurements of Singlet Oxygen Generation Using Singlet Oxygen Sensor Green. *J. Fluoresc.* **23**, 41–47 (2013).
44. Prasad, A., Sedlářová, M. & Pospíšil, P. Singlet Oxygen Imaging Using Fluorescent Probe Singlet Oxygen Sensor Green in Photosynthetic Organisms. *Sci. Rep.* **8**, 13685 (2018).
45. He, X. J. et al. A Vehicle-Free Antimicrobial Polymer Hybrid Gold Nanoparticle as Synergistically Therapeutic Platforms for Staphylococcus aureus Infected Wound Healing. *Adv. Sci.* **9**, 2105223 (2022).
46. Yang, Z. H. & Ming, X.-F. Functions of Arginase Isoforms in Macrophage Inflammatory Responses: Impact on Cardiovascular Diseases and Metabolic Disorders. *Front. Immunol.* **5**, 533 (2014).
47. Wang, H. Y. et al. A Dual-Targeted Organic Photothermal Agent for Enhanced Photothermal Therapy. *Angew. Chem. Int. Ed.* **58**, 1057–1061 (2019).
48. Shao, J. D. et al. Black-Phosphorus-Incorporated Hydrogel as a Sprayable and Biodegradable Photothermal Platform for Postsurgical Treatment of Cancer. *Adv. Sci.* **5**, 1700848 (2018).